JOURNAL OF AIRCRAFT
Vol. 48, No. 1, January–February 2011

Recovery of Energy from Leading- and Trailing-Edge Vortices in Tandem-Airfoil Configurations

D. Rival,* G. Hass,† and C. Tropea‡
Technische Universität, Darmstadt, D-64287 Darmstadt, Germany

DOI: 10.2514/1.C031062

In this study the aerodynamic interactions between tandem pitching and plunging airfoils, inspired by dragonfly flight, were investigated at $Re = 30,000$. The primary parameter to be varied was the phase angle between fore and hindfoils ψ. The aerodynamic interactions were investigated numerically using the unsteady Reynolds-averaged Navier–Stokes equations as well as experimentally in a wind tunnel with the aid of particle image velocimetry. The numerical simulations proved to be reliable in the prediction of the positions and intensities of the shed vortices. Two major aerodynamic interactions were detected. The first type of interaction occurred when the forefoil leading-edge vortex induced a separation on the lower surface of the hindfoil. This was observed for airfoil phasings with $\psi = 60$, 90, and 120°. This vortex-induced separation exerted a strong suction forward and downward and was responsible for high, instantaneous values of thrust. The second type of interaction was observed when the forefoil trailing-edge vortex induced a separation on the upper surface of the hindfoil at airfoil phasings of $\psi = 0$, 30, and 60°. This localized separation exerted a relative strong suction normal to the airfoil surface, increasing the lift as well as the drag. Moreover, this second form of vortex-induced separation over the airfoil upper surface allowed for instantaneous energy extraction on the hindfoil upstroke, i.e., energy recovery.

Nomenclature

C_P	=	nondimensional power
c	=	airfoil chord
c_l	=	sectional lift coefficient
c_d	=	sectional drag coefficient
f	=	frequency
h	=	plunge amplitude
k	=	reduced frequency, $\pi f c/U_\infty$
p	=	pressure
Re	=	Reynolds number, $U_\infty c/\nu$
Re_t	=	turbulent Reynolds number
t	=	period
u	=	streamwise velocity
v	=	normal velocity
x	=	streamwise direction
y	=	normal direction
α	=	angle of attack
α_o	=	mean angle of attack
α_1	=	amplitude of angle of attack
α^*	=	low Reynolds number coefficient
γ	=	angular frequency, $2\pi f$
δ_{ij}	=	Kronecker delta
ν	=	kinematic viscosity
ν_t	=	eddy viscosity
ϕ	=	phase between pitch and plunge
ψ	=	airfoil phasing
ω	=	vorticity

Subscripts

F	=	forefoil
H	=	hindfoil
i, j	=	indices

Presented at the 2010 AIAA Atmospheric Flight Mechanics Conference, Toronto, Canada, 2–5 August 2010; received 9 April 2010; revision received 19 July 2010; accepted for publication 20 July 2010.

*Institute of Fluid Mechanics. Currently, Assistant Professor, Department of Mechanical and Manufacturing Engineering, University of Calgary, Calgary, Alberta, Canada; derival@ucalgary.ca.

†Institute of Fluid Mechanics. Currently, Development Engineer, Thermodynamic Cycles, Thermal Integration and Performances Division, Alstom Power, Baden, Switzerland; guillermo.hass@power.alstom.com.

‡Professor, Institute of Fluid Mechanics.

I. Introduction

BIOLOGISTS over several decades have examined the specific wing kinematics of dragonflies and have uncovered distinct patterns associated with various flight maneuvers [1–6]. It has been observed that at these Reynolds numbers, where laminar boundary-layer separation is unavoidable, dragonflies must use highly separated flows, particularly during the downstroke, to generate the necessary lift during the cycle [7]. Very little regarding the aerodynamic mechanisms themselves could, however, be extracted from these above-mentioned studies. Although present day dragonflies fly with Reynolds numbers on the order of $Re = \mathcal{O}(10^3)$, dragonflies from the Carboniferous and Permian periods, such as *Meganeuropsis permiana* with its giant wingspan up to 75 cm, flew well into the (laminar-to-turbulent) transitional Reynolds number regime [8]. Thus, dragonfly scaling and their overall efficient and highly maneuverable flight provide a source of great inspiration to aerodynamicists struggling to uncover the nuances of biological flight and design efficient micro air vehicles (MAVs).

Over the past decades a great deal of analytical, numerical and experimental investigations into tandem-wing aerodynamics, almost exclusively for hover conditions, have been performed with the hope of better understanding the complex aerodynamic interaction associated with dragonfly flight. Among these, certain investigations have considered the problem from a two-dimensional standpoint with either the assumption of inviscid or laminar flow [9–12]. Others, however, investigated the interaction in three dimensions, primarily using force measurements and to a lesser extent using PIV [13–18]. Certain researchers have shown that through wake capture, large increases in performance are attainable for single wings flapping independently, suggesting that the tandem interaction is only secondary in importance [19–22], in which some go as far as arguing that dragonfly flight is a function of single-wing wake capture and not of vortex interaction between two staggered wings. In contrast it has been shown that even for static tandem configurations at low Reynolds numbers, drag reduction and lift augmentation exists for several stagger and gap configurations [23].

Thus a very broad range of explanations for the unsteady aerodynamic mechanisms in dragonfly flight have been proposed, where some claim that the performance is linked to the stabilization of the spanwise (three-dimensional) flow in the leading-edge vortex (LEV) [18,24]. Conversely, it has been argued that dragonflies use a quasi two-dimensional dynamic stall mechanism [7], with a LEV over the airfoil on the downstroke and attached flow on the upstroke, as shown by the topology in Fig. 1. Thus, by no means does a universal explanation for the unsteady aerodynamic mechanisms associated with dragonfly flight exist at the present time. Thus in this study the authors attempt to elucidate some of the basic aerodynamic mechanisms present in forward-flight conditions.

II. Background

When evaluating the performance of a propulsive system, one usually considers the overall propulsive efficiency defined as:

$$\eta_P = \frac{tU_\infty}{P} \tag{1}$$

where t is the thrust, U_∞ the velocity of the system, and P the power exerted on the surrounding fluid. It therefore becomes clear that to maximize the propulsive efficiency, one needs to simultaneously address the two independent quantities of thrust and power. These two factors in the context of unsteady tandem configurations will now be discussed, first examining thrust production through *leading-edge suction* and then power reduction through *normal suction*.

A. Thrust Production

Knoller [25] and Betz [26] were the first to postulate that a plunging symmetric airfoil can create not only lift but also thrust, generalizing this effect as a consequence of the horizontal component of the lift force when the airfoil is plunged up or down, as shown in Fig. 2. Katzmayr [27] subsequently verified the so-called *Knoller-Betz* effect in his wind-tunnel experiments, where he measured the thrust force exerted on an airfoil in an unsteady wake.

Schmidt [28] tested a tandem-airfoil configuration, as shown in Fig. 3, in which the wake of the rotating forefoil was used to produce thrust on the static hindfoil. This propulsion system was referred to as a *Wellpropeller*, translated as wave propeller. Using a hindfoil profile geometry with a maximum thickness-to-chord ratio of $t/c = 0.25$, the best results were achieved. Compared with conventional airfoils the relatively thick profile was beneficial in creating high thrust forces through the so-called leading-edge suction effect. This suction region, which is developed through a strong flow acceleration at the leading edge, is described in detail for the case of static airfoils [29]. Although Schmidt's experiments were performed at reduced frequencies of $1 \leq k \leq 4$, i.e., at one order of magnitude higher than the experiments in this study, the goal to develop leading-edge suction remains the same.

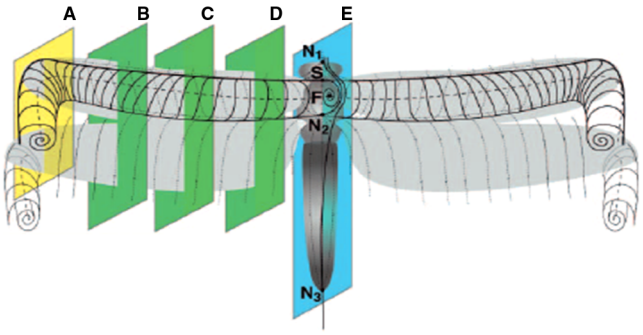

Fig. 1 Topology of LEV on dragonfly forewings, from Thomas et al. [7].

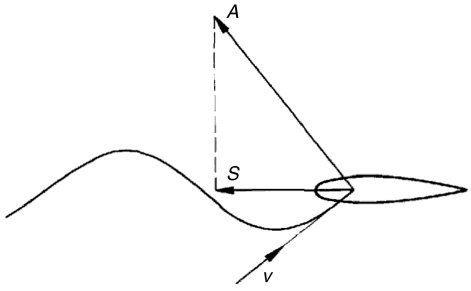

Fig. 2 Creation of thrust on a plunging airfoil, where A is the lift force and S is the resulting horizontal component; taken from Schmidt [28].

Warkentin and DeLaurier [30] tested a tandem-wing ornithopter configuration with reduced frequencies in the range of $0.4 \leq k \leq 1$. They found that a close spacing of approximately one chord length between the wings and phase angles between $\psi = 0$ and 50° were most beneficial for thrust efficiency. A synergy due to the tandem-wing interactions was obtained such that the propulsive efficiency was at times double that of the single-airfoil reference case, even when taking the larger reference area of the tandem arrangement into consideration. Furthermore it was hoped that asymmetric flapping at phase angles of $\psi = 180°$ would produce high thrust efficiencies and simultaneously minimize vertical accelerations for a given MAV design. Unfortunately this phasing presented a substantial drop in performance. Significant leading-edge suction for a static hindwing, based on Schmidt's wave-propeller configuration, could not be achieved in this experiment. A possible explanation for this is the geometry of the thin membrane wings used in the study with their sharp leading edges, thus not providing the necessary surface area for the suction force. As in the case of Schmidt's experiments [28], again no details pertaining to the flowfield at the hindwing leading edge were measured.

B. Power Reduction

The aerodynamic power consumption for a pitching and plunging airfoil over a given period T is defined as:

$$P = \frac{1}{T}\int_T (L\dot{h} + M\dot{\alpha})\,\mathrm{d}t \tag{2}$$

where the moment M can be neglected in this study due to the relatively low-pitch velocities $\dot{\alpha}$, which account for less than 10% of the total power in the most extreme case. Subsequently the non-dimensional power coefficient can be defined as follows:

$$C_P = \frac{2P}{\rho U_\infty^3 c} \tag{3}$$

Akhtar et al. [31] and Lauder et al. [32] showed that bluegill sunfish could modify their thrust production but also their side forces through the interaction of the dorsal-fin wake on the tail fin. During a distinct phasing between the two fins, the effective angle of attack could be increased at the tail fin such that a much stronger LEV was established. The stronger LEV was found to increase the suction on the side of the fin. Similarly the studies by Gopalkrishnan et al. [33] revealed vortex energy capture by a foil in the wake of a D-shaped cylinder, mimicking the behavior of trout in fast-moving water. Here particular modes of vortical interaction were observed such that the vortices from the cylinder interacted with the vortices shed by the foil. For the case of *destructive interaction*, cylinder vortices were repositioned and weakened by vorticity produced by the foil, thus maximizing propulsive efficiency. As a follow-up to this work, Beal et al. [34] showed that euthanized trout (or an analogous passively-mounted foil) could travel upstream (produce thrust) without any power input. This passive propulsion was possible through simple reorientation of the oncoming vortical energy shed from the upstream cylinder. This latter study is an excellent example of how both thrust production through leading-edge suction and vortical-energy extraction through normal suction are coupled and strongly dependent on vortex-airfoil phasing.

III. Parameter Space

The plunging movement of the forefoil F and the pitching/plunging motion of the hindfoil H can be described through Eqs. (4–6), where the hindfoil leads the forefoil with a phase angle ψ:

$$h_F = h\cos(\gamma t) \tag{4}$$

$$h_H = h\cos(\gamma t + \psi) \tag{5}$$

$$\alpha_H = \alpha_o + \alpha_1\cos(\gamma t + \phi + \psi) \tag{6}$$

The forefoil followed a pure-plunging motion with a fixed geometric angle of attack of $\alpha = 8°$. For the hindfoil, pitching lead plunging by a phase angle of $\phi = 90°$ to ensure optimal thrust efficiency [35]. The rotation point for the hindfoil was fixed at the quarter-chord position as this was considered to be a safe extension from classical theory. The dimensionless plunge amplitude for both fore and hindfoils was maintained at $h = \pm 0.5c$. Airfoil spacing was set to $S = 2c$ between the airfoil quarter-chord positions because this close proximity guaranteed strong aerodynamic interference and it was expected that larger spacings would show similar effects but with a phase shift and likely lower intensities. Thus the main parameter to be varied in this study was the phasing between the airfoils (ψ). In Table 1 values for all motion parameters are provided.

IV. Experimental Setup

The PIV measurements were carried out in the Eiffel-type wind tunnel at the Institute of Fluid Mechanics and Aerodynamics (TU Darmstadt). The test section of this low-speed wind tunnel has a cross section of 45 by 45 cm and a length of 2 m. Furthermore the tunnel has a contraction ratio of 24:1 with five turbulence filters in the settling chamber and produces turbulence levels on the order of 1.0% at this study's test speed of 3.75 m/s. The freestream velocity was controlled via closed-loop control, with the tunnel speed input obtained from a hot-wire anemometer (Dantec Dynamics A/S type 55P11) positioned at the entrance of the test section. The hot-wire anemometer was calibrated for each new set of measurements using a miniature vane anemometer.

Both carbon-fibre SD7003 wall-spanning airfoils selected for the wind-tunnel measurements were asymmetric SD7003 profiles with $0.09c$ maximum thickness. The SD7003 profile was used because a substantial experimental database is available for validation in the open literature, such as in Ol et al. [36]. Four linear motors of type LinMot PS01-48x240F-C were used to drive the pitch/plunge motions. External position sensors were mounted on the motor units for higher positional accuracy, allowing for a displacement accuracy of ≤ 0.5 mm and a dynamic angle of attack accuracy of less than 0.5°. All experiments were performed at a physical frequency of $f = 2.5$ Hz equivalent to $k = 0.25$, where the reduced frequency is defined as:

$$k = \frac{\pi f c}{U_\infty} \tag{7}$$

A commercial PIV system was used in this study (Dantec Dynamics A/S) and consisted of a Nd:YAG ($\lambda = 532$ nm) Litron dual-cavity laser with a maximum power output of 135 mJ per cavity and two

Table 1 Values of all motion parameters used throughout the tandem-airfoil simulations

Parameter	Value
Re	30,000
k	0.25
h	$\pm 0.5c$
S	$2c$
α_o	8°
α_1	8.42°
ϕ	90°
ψ	0, 30, 60, 90, and 120°

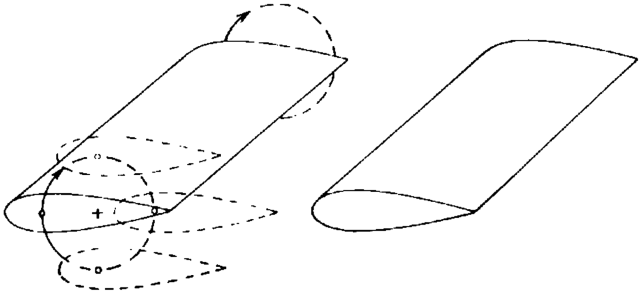

Fig. 3 Arrangement and kinematics of airfoils used for the wave-propeller experiments; taken from Schmidt [28].

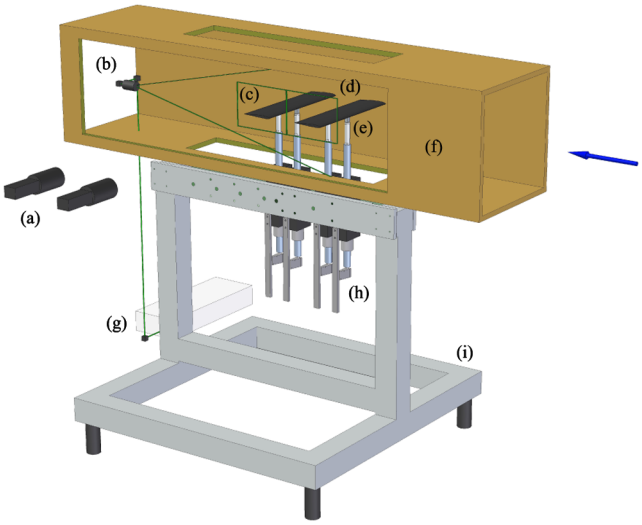

Fig. 4 Experimental setup in wind tunnel with flow direction from right-to-left: a) CCD cameras, b) beam expander, c) PIV image frames, d) wall-spanning carbon-fibre profiles, e) embedded piezo-electric force sensors, f) test-section, g) laser head, h) linear motors with linkage system, and i) base structure.

10-bit FlowSense 2M CCD cameras each with a 1600×1200 pix resolution. Because of the large imaging field required, 60 mm $f/2.8$ Nikkor lenses were used. With the use of compressed air driven through four Laskin nozzles, DEHS seeding particles less than 1 μm in diameter were introduced into the settling chamber using a vertical rake aligned with the measurement plane. The tandem-airfoil configuration in the wind tunnel with PIV setup is shown in Fig. 4. Despite the integration of force sensors, it should be noted here that no direct force measurements were possible at these high reduced frequencies. For more information on the challenges of direct force measurements at high reduced frequencies please refer to Rival and Tropea [37].

PIV image pairs were sampled at 15 Hz allowing for 6 phases to be recorded per cycle at $k = 0.25$. To construct the ensemble velocity fields of 12 phases per cycle, two staggered sets with 100 images per phase were ensemble-averaged. In all cases the first two starting cycles were removed from all ensembles. Each camera imaged a field corresponding to $x/c = 2$ and $y/c = 1.5$, with a resolution of 800 pix/c (6.7 pix/mm). Reflections on the model surface were strongest at the bottom of the stroke where a region $0.04c$ normal to the airfoil surface was deemed to be unreliable. Shadows and strong reflections on the pressure (lower) side required masking. Parallax effects were strongest at the top of the stroke and at this position were responsible for hiding a region $0.03c$ normal to the airfoil surface. The vector fields were calculated using an adaptive correlation with 32×32 pix interrogation windows and a 50% overlap. A 3×3 filter was used to lightly smooth the vector fields to more clearly define the vortical structures in the wake. A local neighborhood validation using a 9×9 moving-average filter and an acceptance factor of 0.2

was employed to eliminate outliers. This, however, also had the effect of smoothing the velocity gradients, thereby thickening the shear layers by approximately $0.05c$.

The accuracy of the vector fields was estimated to lie well below 2% of the freestream velocity ($U_\infty = 3.75$ m/s) for all cases, assuming a maximum subpixel interpolation accuracy of 0.2 pix [38]. Because of the coarse measurement resolution and the low vector overlap (50%), neighboring vectors were assumed to be weakly correlated. Subsequently the vorticity, calculated using a central-differencing scheme, could be estimated to have an uncertainty of $\Delta\omega c/U_\infty = \pm 0.5$ [38].

V. Numerical Simulations

A. Governing Equations

All simulations in this study were performed using the commercial computational fluid dynamics (CFD) solver Fluent 6.3.26. The two-dimensional, incompressible and isothermal unsteady Reynolds-Averaged Navier–Stokes (URANS) Eqs. (8) and (9) were solved using the finite volume method and are presented here in differential form:

$$\frac{\partial \bar{u}_i}{\partial x_i} = 0 \tag{8}$$

$$\frac{\partial \bar{u}_i}{\partial t} + \frac{\partial(\overline{u_i u_j} + \overline{u_i' u_j'})}{\partial x_j} = \frac{\partial}{\partial x_j}\left[\nu\left(\frac{\partial \bar{u}_j}{\partial x_i} + \frac{\partial \bar{u}_i}{\partial x_j}\right)\right] - \frac{1}{\varrho}\frac{\partial \bar{p}}{\partial x_i} \tag{9}$$

where the Reynolds stress term ($\overline{u_i' u_j'}$) is related to the mean velocity field through the Boussinesq approximation:

$$-\overline{u_i' u_j'} = \nu_t\left(\frac{\partial \bar{u}_i}{\partial x_j} + \frac{\partial \bar{u}_j}{\partial x_i}\right) - \frac{2}{3}k\delta_{ij} \tag{10}$$

Closure was performed using the supersonic transport (SST) k-ω turbulence model developed by Menter et al. [39]. To accommodate the transitional Reynolds number regime, the computations were run fully turbulent but fitted with a low-Reynolds number correction, in which the eddy viscosity is dampened using the low-Reynolds number coefficient α^* [40]:

$$\nu_t = \alpha^* \frac{k}{\omega} \tag{11}$$

where the damping coefficient is defined as:

$$\alpha^* = \frac{0.024 + Re_t/6}{1 + Re_t/6} \tag{12}$$

B. Discretization

All simulations were run with a full second-order upwind spatial and first-order temporal discretization, where the latter was limited by the dynamic meshing process. To compensate for this limitation in the temporal discretization, fine time-stepping of 0.5 ms was used, equivalent to 800 time steps per cycle for $k = 0.25$. Further refinement of the time-stepping was performed for a single-airfoil case to check for a time-step independent solution analogous to the grid-independency tests described in the following section. Depending on the reduced frequency of the simulation, 20–30 iterations were run for a given time step with a convergence criterion based on residuals dropping $\mathcal{O}(10^{-4})$ in magnitude. Because the time steps used in the simulations were relatively fine, this convergence criterion was found to be more than ample. Pressure-velocity coupling was performed using the SIMPLE scheme. For all simulations the procedure was to run one complete cycle to establish the appropriate initial conditions and then to begin recording data on the following cycle. This procedure was deemed acceptable after running simulations with multiple cycles for the single-airfoil case and finding no changes in the airfoil lift and drag coefficients in subsequent cycles.

C. Mesh

The numerical domain was modeled after the TU Darmstadt Eiffel-type open-return, closed test-section wind tunnel; see Sec. IV. The inclusion of the encompassing wind-tunnel walls was deemed to be prudent even though maximum static blockage was less than 3%. The domain extends the entire length of the wind-tunnel test section. The forefoil quarter-chord sits $x/c = 7.25$ downstream of the velocity-inlet boundary where equivalent wind-tunnel levels of turbulence were prescribed. For this study's particular airfoil spacing of $S = 2c$ the hindfoil's quarter-chord lies at approximately $x/c = 8.15$ upstream of the pressure-outlet boundary. The domain is filled with block-structured cells in sections a) and d) before and after the dynamic meshing region, as shown in Fig. 5. In these block-structured regions the skewness is zero, and the aspect ratio and cell growth are nearly one.

The circular-core zones surrounding the airfoils provide for the pitching movement (through nonconformal boundaries) whereas the plunging movement was realized through the dynamic-layering method where rows of structured cells above and below the circular cores were created and destroyed depending on the movement. This process can be better understood when examining the middle section of the domain more closely, as shown in Fig. 6. The two unstructured regions in the entire mesh were filled with quadrilateral cells, providing the coupling of the nonconformal boundaries between the circular cores and the block-structured outer region.

Both airfoil and wind-tunnel wall boundary layers were fully resolved satisfying the $y^+ \leq 1$ condition throughout. Cell growth in all boundary layers was limited to 1.25. The trailing edges of the airfoils were set with radii of 0.1 mm so as to be more representative of actual experimental airfoils as well as to ease the meshing constraints. An overall maximum skewness of 0.41 and maximum aspect ratio of 4.1 existed within the circular cores. A complete grid-independency study was performed and a resulting grid of approximately 32,000 cells was established. In Fig. 7 the pressure distribution for a single airfoil at $\alpha = 8^\circ$ with various mesh refinements is shown. The relatively low number of cells and thus fast simulation times (on the order of 6 hours on a single Linux machine) can be greatly attributed to the nearly complete block-structured mesh.

D. Validation

The present numerical model has been previously validated against experimental data for a Reynolds number of $Re = 60,000$ and for reduced frequencies of $0.05 \leq k \leq 0.1$ [41]. Validation for

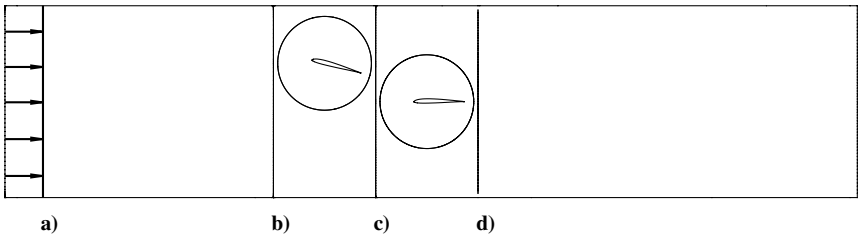

Fig. 5 Numerical domain representative of wind-tunnel test section with forefoil quarter-chord situated at $x/c = 7.25$ downstream of inlet; zones a) and d) contain pure block-structured cells whereas zones b) and c) contain dynamic layering and sliding zones.

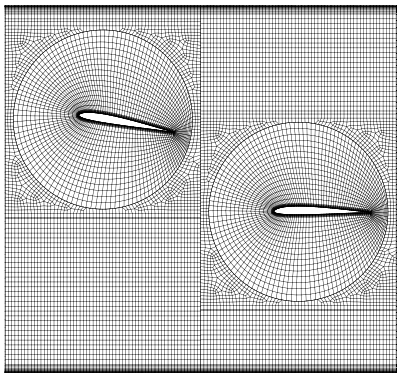

Fig. 6 Middle of numerical domain, zones b) and c), with two circular-structured cores encompassing the airfoils; note airfoils and wind-tunnel walls (top and bottom) with fully resolved boundary layers.

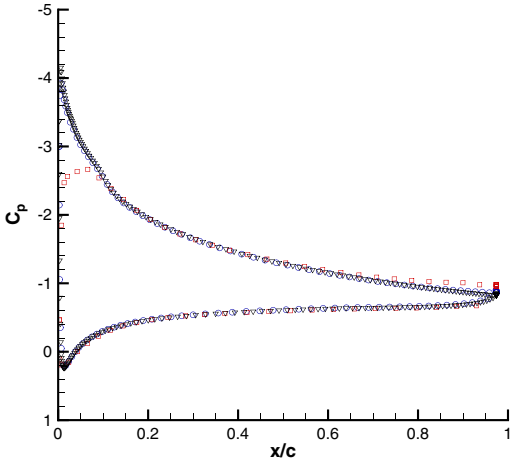

Fig. 7 Effect of grid refinement on pressure distribution for single, static airfoil at $\alpha = 8^{\circ}$; note three levels correspond to meshes with 10,000 cells (□), 28,000 cells (○), and 95,000 cells (∇).

the two single-airfoil reference cases have been presented here using existing force measurements [36]. The comparison for the first reference case, the pure-plunge motion used for the forefoil, is presented in Fig. 8. The agreement of lift with existing force measurements is good, although stall occurs later and more drastically in the simulations as observed by the larger lift peaks at approximately $t/T = 0.3$. Reynolds number sensitivity is very low due to the leading-edge-type separation exhibited for this motion [42]. In the laminar simulation, the shed LEV and trailing-edge vortex (TEV) do not dissipate as quickly and therefore a waviness in the forces, particular strong for drag, can be observed.

When examining the second reference case, the pitch/plunge motion used for the hindfoil, much lower levels of stall are present in both experiment and simulation, see Fig. 9. The Reynolds number sensitivity is thus stronger because the separation/reattachment processes are more influenced to the local pressure gradient. Again the laminar simulations display significant lift- and drag-force fluctuations on the downstroke attributed to the weaker dissipation of the vortical structures developing at both leading- and trailing edges.

Contour plots of dimensionless vorticity are qualitatively compared between experiment and simulation. Dominant vortical structures such as the LEV and TEV are well-captured for the pure-plunge reference case as shown in Figs. 10 and 11. The level of dissipation in both the shed vortex structures as well as for the vortex sheets also appears to be in good agreement.

VI. Results and Discussion

A. Vortex Interaction

Two major vortical interactions have been identified in this study. The first type of interaction occurs when the forefoil leading-edge vortex induces a separation on the lower surface of the hindfoil. This was observed for airfoil phasings with $\psi = 60°$, $\psi = 90°$ and $\psi = 120°$. This vortex-induced separation exerted a strong suction forward and downward and was responsible for high, instantaneous values of thrust. The second type of interaction was observed when the forefoil trailing-edge vortex induces a separation on the upper surface of the hindfoil at airfoil phasings of $\psi = 0°$, $\psi = 30°$ and $\psi = 60°$.

Figures 12 and 13 show exemplarily the lift and drag variations for the tandem arrangements with $\psi = 60°$ and $\psi = 90°$, respectively. For comparison, the force variations for the single reference cases are also plotted. It is found that the tandem arrangement has a minor influence on the forefoil lift and drag, with slightly higher variations in the case of the downstroke. However, the vortex interaction on the hindfoil upstroke for $\psi = 60°$ and $\psi = 90°$ can be clearly identified at approximately time steps $t/T = 0.583$ and $t/T = 0.667$, respectively. Note that the time axis has been shifted for the hindfoil to ease the comparison with the reference cases. Of significance here is the added lift on the upstroke for $\psi = 60°$, as shown in Fig. 12a. Also of particular benefit is the strong leading-edge suction leading to thrust for $\psi = 90°$, seen by a significant drop in drag in Fig. 12b.

B. Thrust Production

When examining the contour plots of vorticity at $t/T = 0.417$ in Fig. 14 (these correspond to $t/T = 0.583$ and $t/T = 0.667$ in Figs. 12 and 13 due to the shifting of time axis) one can clearly

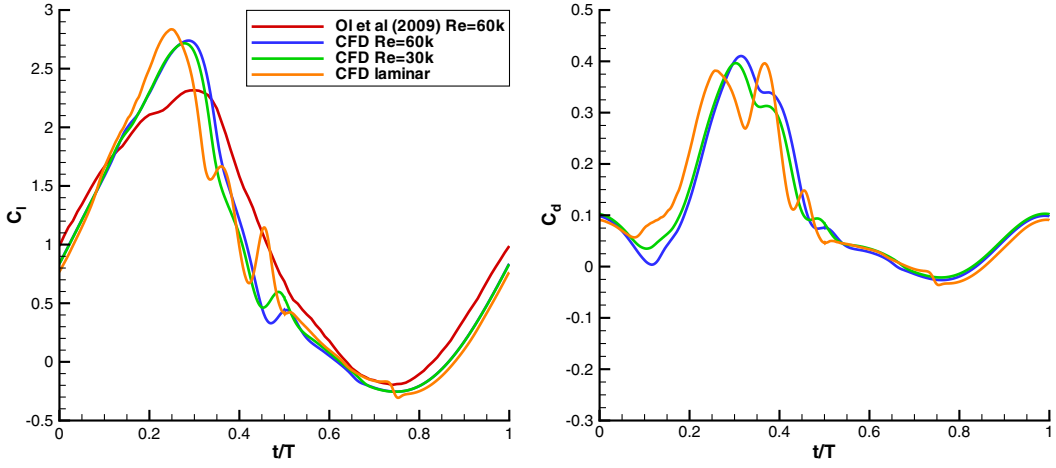

a) Lift **b) Drag**

Fig. 8 Validation of lift and drag for the pure-plunge reference case used for forefoil; note reference data taken from experiment by OI et al. [36].

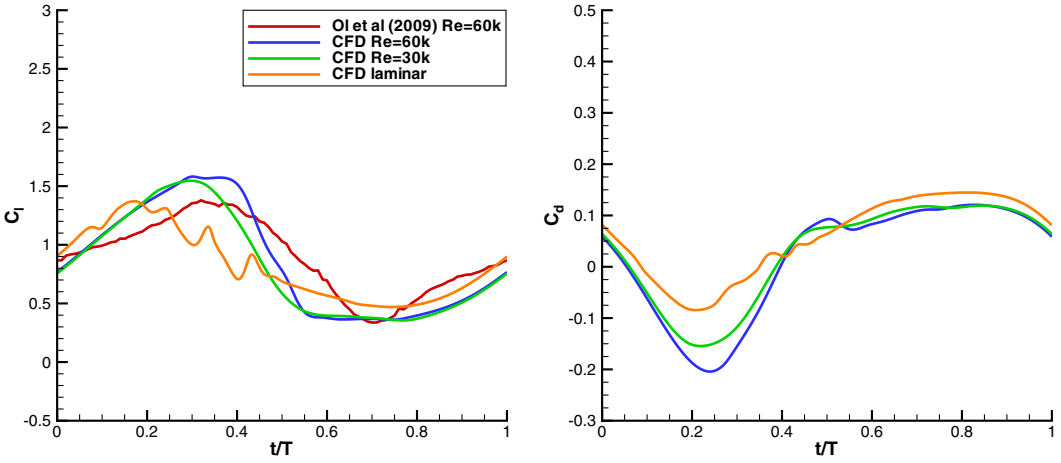

Fig. 9 Validation of lift and drag for pitch/plunge reference case used for hindfoil; note reference data taken from experiment by Ol et al. [36].

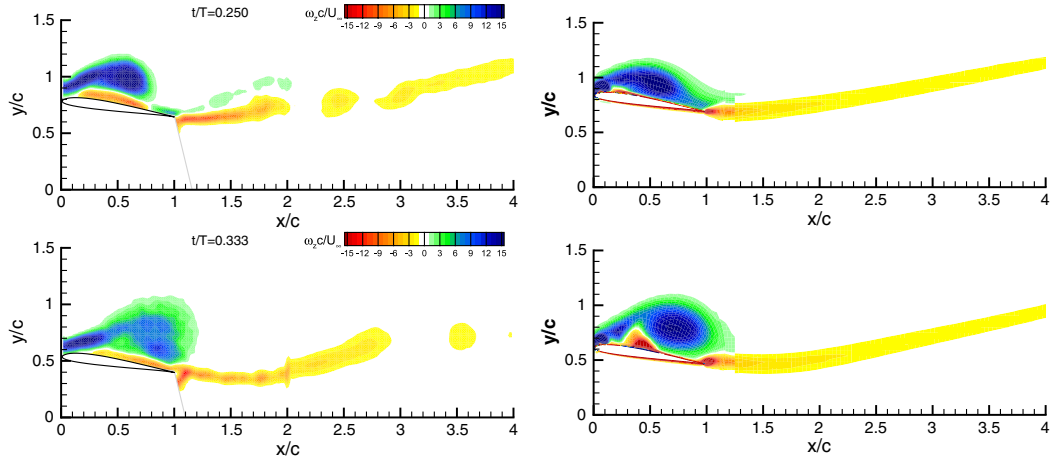

Fig. 10 Comparison between the experiment (left) and CFD (right) for the pure-plunge reference case at the middle of the downstroke ($t/T = 0.250$) and at one time step later ($t/T = 0.333$).

observe the suction regime just below the hindfoil leading edge. The approaching LEV's downwash induces a leading-edge vortex at this position thus generating the strong thrust force. This suction region is particularly noticeable for the $\psi = 90°$ case. In the PIV measurements, the shadow conceals this suction region. Even without the presence of this shadow, laser reflections at the airfoil surface would limit the accuracy of the velocity measurements in this region. Thus the numerical simulations provide insight into the vortical interactions in compliment to the experiment.

C. Power Reduction

The timing of the normal force relative to the airfoil plunge velocity becomes critical when considering power consumption.

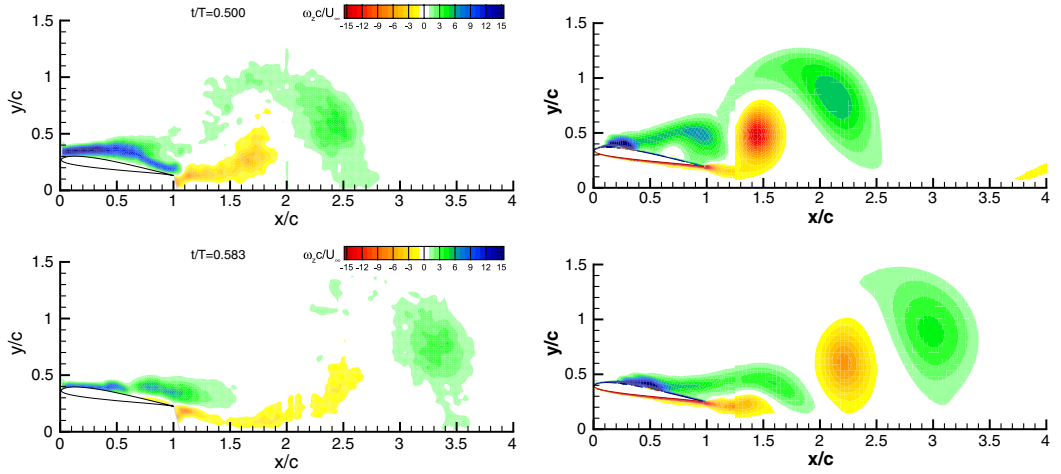

Fig. 11 Comparison between the experiment (left) and CFD (right) for the pure-plunge reference case at the bottom of the downstroke ($t/T = 0.5$) and at one time step later ($t/T = 0.583$).

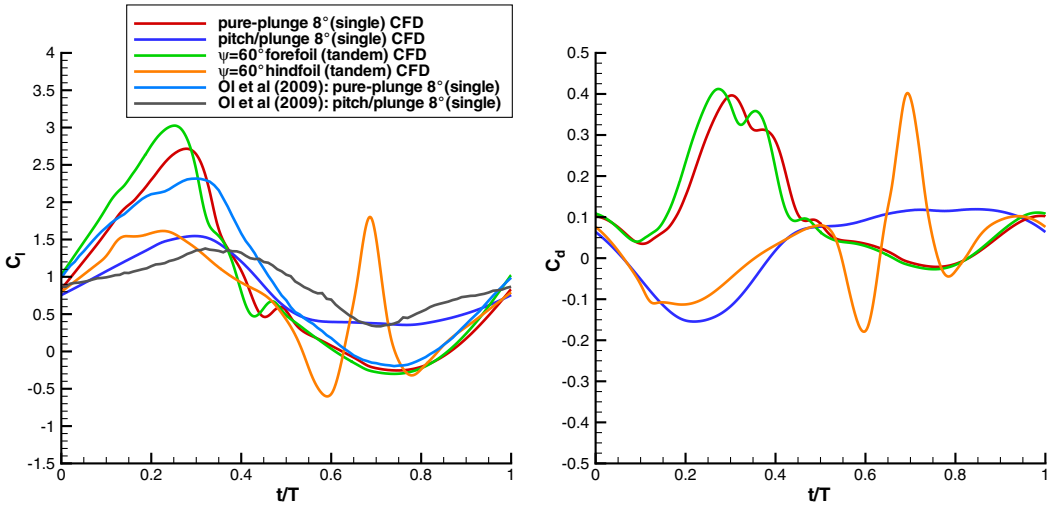

a) Lift b) Drag

Fig. 12 Lift and drag variation for tandem arrangement at $\psi = 60°$; observe increase in lift and drag at approximate time step $t/T = 0.667$ followed by overshoot, note hindfoil curve shifted in time for comparison.

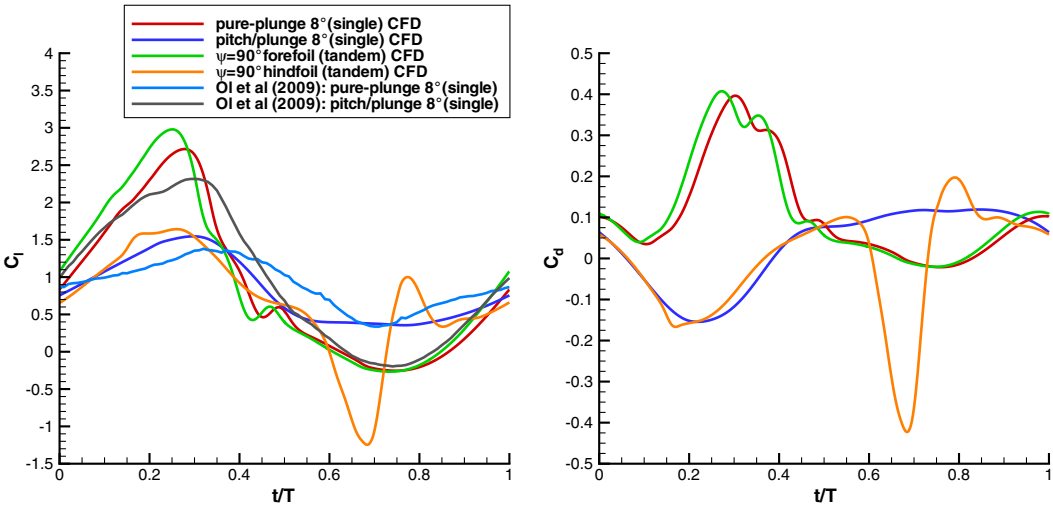

a) Lift b) Drag

Fig. 13 Lift and drag variation for tandem arrangement at $\psi = 90°$; observe drop in lift and drag at approximate time step $t/T = 0.667$, note hindfoil curve shifted in time for comparison.

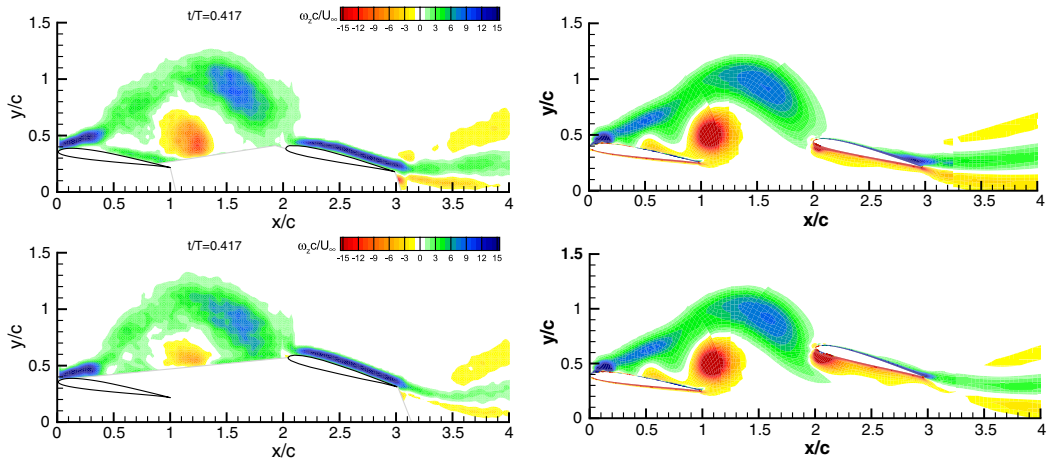

Fig. 14 Development of leading-edge suction on forefoil for $\psi = 60°$ (top) and $\psi = 90°$ (bottom): experiment (left) and CFD (right), where time is referenced to forefoil motion. Note leading-edge suction in experiment not visible due to shadow.

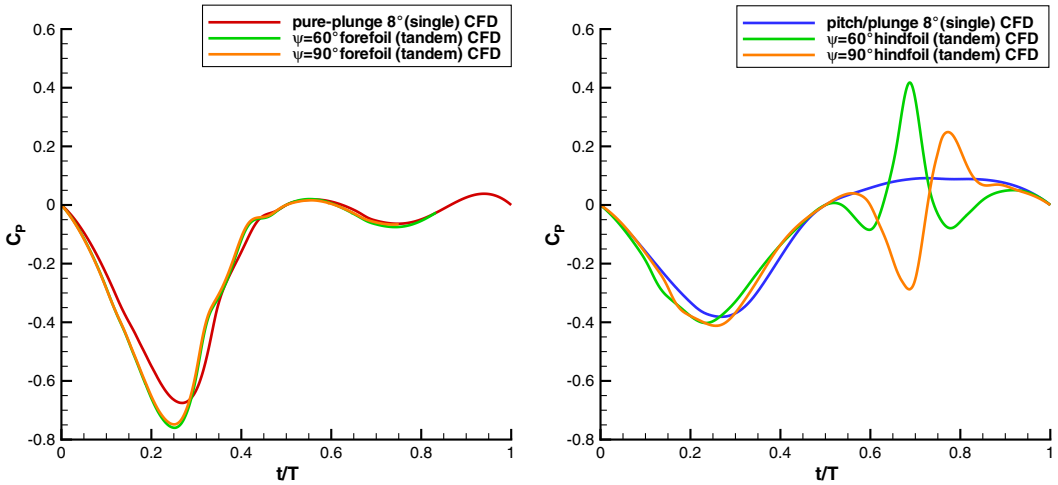

Fig. 15 Variation in power consumption for tandem arrangements for $\psi = 60$ and 90° where positive C_P refers to energy extraction; note hindfoil curve shifted in time for comparison.

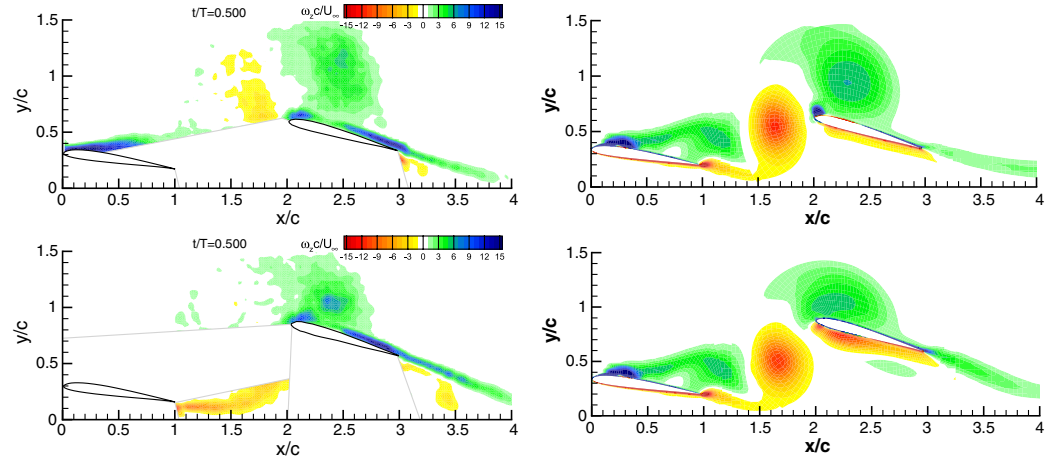

Fig. 16 Interaction of TEV on hindfoil for $\psi = 60$ (top) and 90° (bottom) responsible for suction region near leading edge: experiment (left) and CFD (right), where time is referenced to forefoil motion.

In Fig. 15 it is apparent that a slight increase in power consumption can be observed for the forefoil when compared with the reference case. However, on the hindfoil, the passing of the LEV over the hindfoil upper surface is responsible for suction in the normal direction, of particular benefit for $\psi = 60°$.

Again referring to plots of dimensionless vorticity at the corresponding time step of $t/T = 0.5$ in Fig. 16 ($t/T = 0.667$ and $t/T = 0.75$ in Fig. 15), the suction responsible for reducing power consumption can be observed, both in experiment and CFD. The approaching TEV induces an upwash at the leading edge, in contrast to the downwash effect of the LEV for thrust generation, such that a strong and compact suction region is generated over the suction surface. From these results one can surmise that the timing of such an interaction, when considering power reduction, is very sensitive to the position and plunging velocity of the hindfoil, such that the $\psi = 60°$ case shows a substantial improvement over the $\psi = 90°$ case simply due to the difference in the hindfoil velocity at the time of interaction.

VII. Conclusions

The vortex interaction of two moving airfoils in tandem configuration has been examined both experimentally (PIV) and numerically (URANS) at a Reynolds number of $Re = 30,000$. By varying the airfoil phasing ψ, two types of vortex interactions have been identified. The first type of interaction occurred at $\psi = 60, 90,$ and 120° where the passing LEV from the forefoil induced a leading-edge suction region on the hindfoil. This suction in turn generated added thrust, particularly at $\psi = 90°$. The second type of interaction was observed at $\psi = 0, 30,$ and 60° where the passing TEV induced a separation on the hindfoil upper surface (near the leading edge). In this case, the generation of a normal force on the upstroke allowed for the reduction in power consumption, as shown for $\psi = 60°$.

Acknowledgments

This research was supported by the Deutsche Forschungsgemeinschaft within the national priority program entitled *Nature-Inspired Fluid Mechanics* (SPP1207, Tr 194/40).

References

[1] Norberg, R. A., "Hovering Flight of the Dragonfly Aeschna Juncea L," *Swimming and Flying in Nature*, Vol. 2, Plenum Press, New York, 1975, pp. 763–781.

[2] Alexander, D. E., "Unusual Phase Relationships between the Forewings and Hindwings in Flying Dragonflies," *Journal of Experimental Biology*, Vol. 109, 1984, pp. 379–383.

[3] Azuma, A., Azuma, S., Watanabe, I., and Furuta, T., "Flight Mechanics of a Dragonfly," *Journal of Experimental Biology*, Vol. 116, 1985, pp. 79–107.

[4] Azuma, A., and Watanabe, T., "Flight Performance of a Dragonfly," *Journal of Experimental Biology*, Vol. 137, 1988, pp. 221–252.

[5] Rueppell, G., "Kinematic Analysis of Symmetrical Flight Manoeuvres of Odonata," *Journal of Experimental Biology*, Vol. 144, 1989, pp. 13–42.

[6] Wang, Z. J., and Russell, D., "Effect of Forewing and Hindwing Interactions on Aerodynamic Forces and Power in Hovering Dragonfly Flight," *Physical Review Letters*, Vol. 99, No. 14, 2007, p. 148101. doi:10.1103/PhysRevLett.99.148101

[7] Thomas, A. L. R., Taylor, G. K., Srygley, R. B., Nudds, R. L., and Bomphrey, R. J., "Dragonfly Flight: Free-Flight and Tethered Flow Visualizations Reveal a Diverse Array of Unsteady Lift-Generating Mechanisms, Controlled Primarily via Angle of Attack," *Journal of Experimental Biology*, Vol. 207, 2004, pp. 4299–4323. doi:10.1242/jeb.01262

[8] Beckemeyer, R. J., "Hind Wing Fragments of Meganeuropsis (Protodonata: Meganeuridae) from the Lower Permian of Noble County, Oklahoma," *Bulletin of American Odonatology*, Vol. 9, Nos. 3–4, 2006, pp. 85–89.

[9] Bosch, H., "Interfering Airfoils in Two-Dimensional Unsteady Incompressible Flow," AGARD CP-227, Paper No. 7, 1978.

[10] Lan, S. L., and Sun, M., "Aerodynamic Interactions of Two Airfoils in Unsteady Motion," *Acta Mechanica*, Vol. 150, Nos. 1–2, 2001, pp. 39–51. doi:10.1007/BF01178543

[11] Sun, M., and Lan, S. L., "A Computational Study of the Aerodynamic Forces and Power Requirements of Dragonfly (Aeschna Juncea) Hovering," *Journal of Experimental Biology*, Vol. 207, 2004, pp. 1887–1901. doi:10.1242/jeb.00969

[12] Wang, J. K., and Sun, M., "A Computational Study of the Aerodynamics and Forewing-Hindwing Interaction of a Model Dragonfly in Forward Flight," *Journal of Experimental Biology*, Vol. 208, 2005, pp. 3785–3804. doi:10.1242/jeb.01852

[13] Isogai, K., Fujishiro, S., Saitoh, T., Yamamoto, M., Yamasaki, M., and Matsubara, M., "Unsteady Three-Dimensional Viscous Flow Simulation of a Dragonfly Hovering," *AIAA Journal*, Vol. 42, No. 10, 2004, pp. 2053–2059. doi:10.2514/1.6274

[14] Maybury, W. J., and Lehmann, F.-O., "The Fluid Dynamics of Flight Control by Kinematic Phase Lag Variation Between Two Robotic Insect Wings," *Journal of Experimental Biology*, Vol. 207, 2004, pp. 4707–4726. doi:10.1242/jeb.01319

[15] Yamamoto, M., and Isogai, K., "Measurement of Unsteady Fluid Dynamic Forces for a Mechanical Dragonfly Model," *AIAA Journal*, Vol. 43, No. 12, 2005, pp. 2475–2480. doi:10.2514/1.15899

[16] Usherwood, J. R., and Lehmann, F.-O., "Phasing of Dragonfly Wings Can Improve Aerodynamic Efficiency by Removing Swirl," *Journal of the Royal Society Interface*, Vol. 5, No. 28, 2008, pp. 1303–1307. doi:10.1098/rsif.2008.0124

[17] Lehmann, F.-O., "When Wings Touch Wakes: Understanding Locomotor Force Control by Wake–Wing Interference In Insect Wings," *Journal of Experimental Biology*, Vol. 211, 2008, pp. 224–233. doi:10.1242/jeb.007575

[18] Lehmann, F.-O., "Wing-Wake Interaction Reduces Power Consumption in Insect Tandem Wings," *Experiments in Fluids*, Vol. 46, No. 5, 2009, pp. 765–775. doi:10.1007/s00348-008-0595-0

[19] Savage, S. B., Newman, B. G., and Wong, D. T.-M., "The Role Of Vortices And Unsteady Effects During The Hovering Flight Of Dragonflies," *Journal of Experimental Biology*, Vol. 83, 1979, pp. 59–77.

[20] Gustafson, K., and Leben, R., "Computation of Dragonfly Aerodynamics," *Computer Physics Communications*, Vol. 65, Nos. 1–3, 1991, pp. 121–132. doi:10.1016/0010-4655(91)90163-F

[21] Anderson, J. M., Streitlien, K., Barrett, D. S., and Triantafyllou, M. S., "Oscillating Foils of High Propulsive Efficiency," *Journal of Fluid Mechanics*, Vol. 360, 1998, pp. 41–72. doi:10.1017/S0022112097008392

[22] Birch, J. M., and Dickinson, M. H., "The Influence of Wing-Wake Interactions on the Production Of Aerodynamic Forces in Flapping Flight," *Journal of Experimental Biology*, Vol. 206, 2003, pp. 2257–2272. doi:10.1242/jeb.00381

[23] Scharpf, D. F., and Mueller, T. J., "Experimental Study of a Low Reynolds Number Tandem Airfoil Configuration," *Journal of Aircraft*, Vol. 29, No. 2, 1992, pp. 231–236. doi:10.2514/3.46149

[24] Ellington, C. P., "Insects Versus Birds: The Great Divide," *44th AIAA Aerospace Sciences Meeting and Exhibit*, AIAA Paper 2006-35, 2006.

[25] Knoller, R., "Die Gesetze des Luftwiderstands," *Flug und Motortechnik (Wien)*, Vol. 21, 1909, pp. 1–7.

[26] Betz, A., "Ein Beitrag zur Erklärung des Segelfluges," *Zeitschrift für Flugtechnik und Motorluftschiffahrt*, Vol. 3, 1912, pp. 269–272.

[27] Katzmayr, R., "Über das Verhalten von Flügelflächen bei Periodischen Änderungen der Geschwindigkeitsrichtung," *Zeitschrift für Flugtechnik und Motorluftschiffahrt*, Vol. 13, 1922, pp. 95–101.

[28] Schmidt, W., "Der Wellpropeller, ein neuer Antrieb für Wasser-, Land- und Luftfahrzeuge," *Zeitschrift für Flugwissenschaften und Weltraumforschung*, Vol. 12, 1965, pp. 472–479.

[29] Katz, J., and Plotkin, A., *Low Speed Aerodynamics*, Cambridge Univ. Press, Cambridge, MA, 2001.

[30] Warkentin, J., and DeLaurier, J., "Experimental Aerodynamic Study of Tandem Flapping Membrane Wings," *Journal of Aircraft*, Vol. 44, No. 5, 2007, pp. 1653–1660. doi:10.2514/1.28160

[31] Akhtar, I., Mittal, R., Lauder, G. V., and Drucker, E., "Hydrodynamics of a Biologically Inspired Tandem Flapping Foil Configuration," *Theoretical and Computational Fluid Dynamics*, Vol. 21, No. 3, 2007, pp. 155–170. doi:10.1007/s00162-007-0045-2

[32] Lauder, G. V., Anderson, E. K., Tangorra, J., and Madden, P. G. A., "Fish Biorobotics: Kinematics and Hydrodynamics of Self-Propulsion," *Journal of Experimental Biology*, Vol. 210, 2007, pp. 2767–2780. doi:10.1242/jeb.000265

[33] Gopalkrishnan, F. S., Triantafyllou, M. S., Triantafyllou, G. S., and Barrett, D., "Active Vorticity Control in a Shear Flow Using a Flapping Foil," *Journal of Fluid Mechanics*, Vol. 274, No. -1, 1994, pp. 1–21. doi:10.1017/S0022112094002016

[34] Beal, D. N., Hover, F. S., Triantafyllou, M. S., Liao, J. C., and Lauder, G. V., "Passive Propulsion in Vortex Wakes," *Journal of Fluid Mechanics*, Vol. 549, 2006, pp. 385–402. doi:10.1017/S0022112005007925

[35] Mueller, T. J., *Fixed and Flapping Wing Aerodynamics for Micro Air Vehicle Applications*, AIAA, Reston, VA, 2001.

[36] Ol, M. V., Bernal, L., Kang, C.-K., and Shyy, W., "Shallow and Deep Dynamic Stall for Flapping Low Reynolds Number Airfoils," *Experiments in Fluids*, Vol. 46, No. 5, 2009, pp. 883–901. doi:10.1007/s00348-009-0660-3

[37] Rival, D., and Tropea, C., "Characteristics of Pitching and Plunging Airfoils Under Dynamic-Stall Conditions," *Journal of Aircraft*, Vol. 47, No. 1, 2010, pp. 80–86.

[38] Raffel, M., Willert, C. E., Wereley, S., and Kompenhans, J., *Particle Image Velocimetry: A Practical Guide*, 2nd ed., Springer–Verlag, New York, 2007.

[39] Menter, F. R., Kuntz, M., and Langtry, R., "Ten Years of Experience with the SST Turbulence Model," *Turbulence, Heat and Mass Transfer 4*, Begell House Inc., Redding, CT, 2003, pp. 625–632.

[40] Wilcox, D. C., *Turbulence Modeling for CFD*, DCW Industries Inc., La Canada, CA, 1998.

[41] Rival, D., Dumond, J., and Tropea, C., "Lift Augmentation for Two Pitching and Plunging Airfoils in Tandem Formation," *46th AIAA Aerospace Sciences Meeting and Exhibit, Reno, USA*, AIAA Paper 2008-1441, 2008.

[42] Ekaterinaris, J. A., and Menter, F. R., "Computation of Oscillating Airfoil Flows with One- and Two-Equation Turbulence Models," *AIAA Journal*, Vol. 32, No. 12, 1994, pp. 2359–2365. doi:10.2514/3.12300